Controlling the Coverage of Full Poincaré Beams through Second-Harmonic Generation

Subith Kumar[1,2,*], Ravi K. Saripalli[1,3], Anirban Ghosh[1], Wagner T. Buono[4], Andrew Forbes[4] and G.K. Samanta[1]

[1]*Photonic Sciences Laboratory, Physical Research Laboratory, Navrangpura, Ahmedabad, Gujarat 380009, Republic of India*

[2]*Indian Institute of Technology—Gandhinagar, Ahmedabad, Gujarat 382424, Republic of India*

[3]*Directed Energy Research Centre, Technology Innovation Institute, Abu Dhabi, United Arab Emirates*

[4]*School of Physics, University of the Witwatersrand, Johannesburg 2050, Republic of South Africa*

Ideal full Poincaré (FP) beams contain all possible polarization states on the surface of the Poincaré sphere and are readily created by linear optical techniques and, more recently, by nonlinear optical processes. An inherent limitation in the latter is the inability to achieve all polarization states, coined coverage, due to modal size, polarization, and modal weighting changes during the nonlinear conversion of the constituent modes. Here, we demonstrate a simple technique to control the coverage of FP beams, using second-harmonic generation as an example, from fully scalar (no coverage) to fully vectorial (full coverage). Our method for determining the coverage confirms the vectorial characteristics of the generated beams and reveals a balancing act between mode order, modal nonlinear efficiency, and initial relative modal weights, all in close agreement with that theoretically predicted. Our findings will hopefully be of value to the communities interested in nonlinear structured light, particularly for vectorial nonlinear modal creators and detectors and control of quantum hybrid entangled states.

I. INTRODUCTION

Structured light, including Laguerre-Gauss (LG) modes of light that carry orbital angular momentum (OAM), has been a fast-growing field in recent years due to access to being able to use the spatially varying phase and space degree of freedom [1]. Another popular degree of freedom, the polarization of the light beam, is a consequence of the vectorial nature of the electromagnetic field. Light beams with a spatially varying polarization distribution, known as Poincaré beams [1], can be constructed from a coaxial superposition of an orthogonally polarized fundamental Gaussian mode and an LG mode [2,3]. With the study of beams having a nontrivial distribution of polarization and by exploiting this vectorial nature of light, new dimensions have opened up, since Poincaré beams interaction with matter is polarization sensitive. Such vector light shows promising applications [3–5] in both classical and quantum contexts [6]. Notable vectorial structures of light are full Poincaré (FP) beams [2], which carry all possible polarization states spanning over the entire surface of the Poincaré sphere. Since the demonstration by Beckley *et al.* [2], FP beams have attracted a great deal

of interest in various science and technology applications. The inherent spatial distribution and the flat-top intensity distribution [7] of the polarization states over the transverse plane make the FP beam a good candidate for an on-demand polarization source. It is also well established that the spin and orbital angular momentum of light play an important role in material processing [8], biomedical applications [9], and optical manipulation [10]. The spatial degree of freedom for choosing the spin-orbital angular momentum in FP beams further enhances the usefulness of FP beams in similar applications. For each of these applications, it is essential to properly quantify and control the polarization content of the optical beam at different wavelengths.

On the other hand, the generation of structured beams with spatially varying polarization can be challenging, as it entails an amalgamation of beam-shaping techniques, viz., liquid crystals, spatial light modulators, etc., interferometric setups, and computer resources and algorithms, that altogether make up a complex setup. This can impose certain restrictions: for example, while in theory the FP beam can carry all possible polarization states on the surface of the Poincaré sphere, in practice, due to the finite size of the superposed beams, the generation of an FP beam with full polarization coverage is difficult. Direct

*subithpkumar@gmail.com

generation straight from lasers [11–14] has also been explored. In this regard, the modal description has been a useful tool to describe newly formed structures [15]. However, this type of generation is restricted in wavelength by the availability of gain media. Traditionally, FP beams are generated and controlled by linear optical elements. The nonlinear creation and control of FP beams is a subject that is very much in its infancy [16].

For the case of second-harmonic generation (SHG), seminal works have revealed the interesting effects of topological doubling [13,17], algebra [18], and analysis of the conversion of FP beams [19,20]. Nowadays, in the forefront of this area is the nonlinear behavior of vector light [21], with recent works accessing frequency up-conversion [20,22–25] and down-conversion [26], even in the quantum realm [27].

However, an early aspect of SHG has not been taken into consideration when using FP beams: different optical modes have different conversion efficiencies. This has been debated early in the field with seminal works using Bessel beams [28–32] but the principle is the same, viz., a nonlinear process efficiency is proportional to its intensity, which in turn is the average power over the area. The waist parameter of a structured beam increases in proportion to the square root of its order [33], increasing the minimum area achieved while focused and therefore decreasing the conversion efficiency. A consequence is that FP beams do not remain FP, with the coverage potentially increasing or decreasing depending on both the beam and medium conditions.

In FP beams, the spatial and polarization degrees of freedom are coupled in a nonseparable manner, mimicking the phenomenon of entanglement in quantum mechanics. This coupling will depend on the extent of spatial overlap of the orthogonal polarization and modes. The use of FP beams for material processing [8] can be very useful with regard to the ability to create complex structures and precise features by controlling the polarization and modal distribution in the FP beams. Furthermore, the SHG of FP beams opens up access to the exotic wavelengths [34] where the direct structuring of optical beams is difficult. Recent studies have shown that nonlinear up-conversion is an effective method to tune the wavelength while maintaining its quantum properties [35]. This highlights the usefulness of nonlinear up-conversion to quantum processes that use the polarization degree of freedom in cryptography [36] or hybrid entanglement [37]. In view of the above applications, it is imperative to study the polarization coverage and modal coverage of generated FP beams. In this work, we address this open problem and demonstrate a simple technique to control the coverage of FP beams, from fully scalar (no coverage) to fully vectorial (full coverage). Using SHG in a single-pass dual-crystal geometry with various topological charges as vectorial inputs, we show how the relative weightings and

SHG affect features such as singularities and L lines and analyze how the coverage is affected by the change in beam sizes and different conversion efficiencies for the two constituent modes of an FP beam. We reveal the balancing act between mode order, modal nonlinear efficiency, and initial relative modal weights, all in close agreement with that theoretically predicted.

II. BACKGROUND AND CONCEPT

Full Poincaré beams are generated by the coaxial superposition of orthogonally polarized Gaussian and Laguerre-Gaussian (LG) beams. The electric field expression for the FP beam can be written as $E = \alpha \, |E^H, l\rangle + \beta \, |E^V, 0\rangle$, where α and β are the normalized amplitude coefficients of the LG and Gaussian beams. For the theoretical generation of FP beams, we generate the transverse-electric-field distribution of the horizontal ($|E^H, l\rangle$) and vertical ($|E^V, 0\rangle$) components using the experimental parameters in a two-dimensional (2D) array with the same size of detector-aperture resolution. These transverse-electric-field expressions are further used in calculating the theoretical intensity profile for four different combinations of $\lambda/2$ and $\lambda/4$ wave plates that are sufficient for the measurement of the Stokes parameters. The Stokes parameters, traditionally labeled as S_0, S_1, S_2, and S_3 on the axis of a Poincaré sphere, play a crucial role in visualizing the unconventional polarization states of light beams. These four parameters are sufficient for calculating the ellipse orientation ($\psi = \tan^{-1} S_2/S_1$) and ellipticity ($\chi = \sin^{-1} S_3/S_0$) of the polarization ellipse in both experiment and theory.

To study the polarization topology of the FP beam, we study the singularities in the Stokes field. The Stokes fields are hypothetical complex fields constructed from the Stokes parameters [38], described by $S_{12} = S_1 + iS_2$, $S_{23} = S_2 + iS_3$, and $S_{31} = S_3 + iS_1$. The Stokes phases, the arguments of the Stokes fields, can be calculated as $\phi_{ij} = \tan^{-1} S_j/S_i$, where, $i,j = 1$, 2, and 3. The Stokes vortices are the points in the Stokes-phase field with screw dislocation, often quantified by charge σ_{ij} (the number of 0–2π phase windings around the dislocation). The Stokes phase σ_{12} is used for visualizing C-point polarization singularities, which are the points in the optical fields where the orientation of the polarization ellipse is undefined. C-point singularities are characterized by circular singularity indices I_c, representing the number of complete 2π rotations of the polarization ellipse around the singularity point. Since the ellipse orientation is calculated by $\psi = 1/(2) \tan^{-1} S_2/S_1$, the circular-singularity indices I_c and the Stokes-vortex charge σ_{12} are further related by $\sigma_{12} = 2I_c$ [38,39]. The vortices σ_{23} in the Stokes field, S_{23}, also known as the Poincaré field, represent the net orbital angular momentum of the beam. The number of C-point singularity pairs in the FP beam is the same as the vortex order σ_{23} of the beam.

The coverage of the FP beam on the Poincaré sphere is realized by one-to-one mapping of the polarization calculated in each of the pixels in the detector plane to a point on the surface of the Poincaré sphere. The area then measures the coverage by these points with respect to the total area of the Poincaré sphere. Therefore, the FP beam coverage on the surface of the Poincaré sphere can be considered as the net accessible polarization states available in an FP beam. A coverage of more than 75% of the Poincaré sphere is deemed acceptable for many applications [40]. To understand how these polarization states are generated in the detector plane, let us consider the area where two beams with orthogonal polarizations are spatially overlapping. The areas where the two orthogonally polarized beams do not overlap only contains their respective polarization states. The diverging polarization states

will only exist in the space where these two beams are spatially superimposed and their relative weights and phases will dictate the polarization state at a given position. This spatial overlap of the beams, however, decreases when considering the SHG of both beams. This can be observed in Fig. 1 and can be explained as follows. In the SHG process, while a Gaussian beam generates another Gaussian with a smaller area, a Laguerre-Gaussian (LG) beam also generates an LG beam but with its intensity distribution further away from the center and with a sharper drop in intensity.

In Fig. 1(a), we illustrate the beam-intensity profiles along the overlapping region in black. If this area is projected in the radial direction, as in Fig. 1(b), it is easier to see that the region decreases, particularly if a detection threshold (a minimum total intensity required for practical purposes) is considered. For the case of a Gaussian beam with right-circular polarization and an LG beam with left-circular polarization composing the fundamental or pump wavelength, we illustrate this effect in Fig. 1(c). Circular polarization states are only found in regions where just one beam has a detectable intensity. All other polarization states are confined in between. A linear polarization state can be found in a radial coordinate, where both have equal intensities. In this case, for the fundamental beam, equal weights are used. However, this balance is broken in SHG, where a Gaussian and an LG beam have different conversion efficiencies. The region containing all polarization states decreases, meaning that for a finite detection system, the total number of detectable states also decreases. In Fig. 1(d), we try to mitigate this effect by changing the relative intensities of the fundamental wavelength in order to compensate the conversion efficiency and improve the number of states in the SHG.
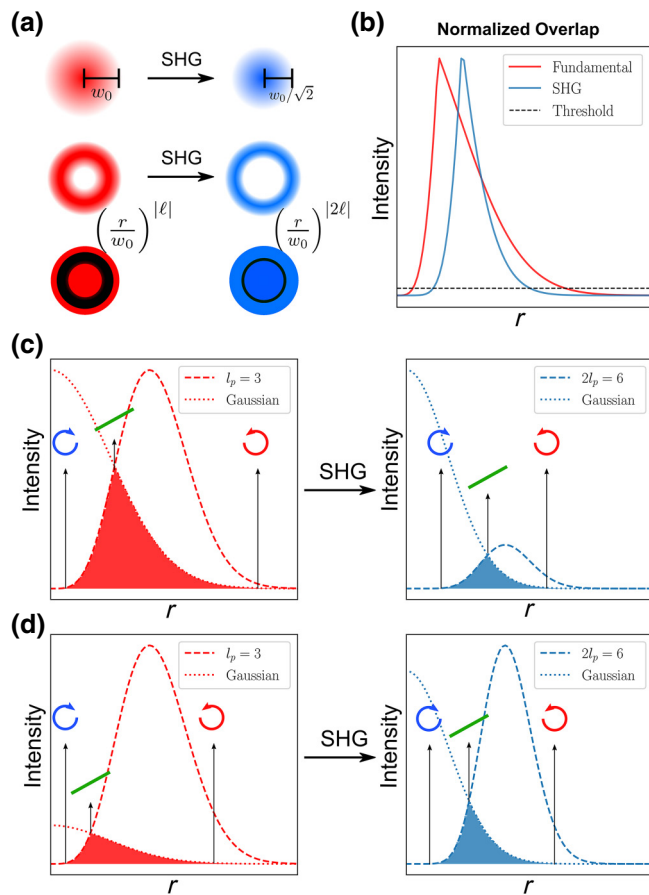

FIG. 1. Spatial overlap and polarization. (a) An illustration of how both constituent spatial modes of an FP beam change differently in size when used in SHG, changing the total overlap area (depicted in black). (b) A projection of both overlaps in the radial direction. (c) The region where the beams overlap can decrease even more if different mode efficiencies are considered. (d) The relative intensities of the fundamental-wavelength beams are adjusted in order to maximize the overlap area of SHG, taking the different modal efficiencies into consideration.

III. EXPERIMENTAL SETUP

The schematic of the experimental setup is shown in Fig. 2. A Ti:sapphire laser delivering (pulse width 17 fs, repetition rate 80 MHz) an average output power of 837 mW is used as the fundamental source. The output radiation has a wavelength of 55 nm, centered at 810 nm. The combination of a $\lambda/2$-plate (HWP1) and a polarizing-beam-splitter (PBS1) cube is used to control the laser power in the experiment. The second $\lambda/2$-plate (HWP2) controls the polarization of the input beam to the polarization-based Mach-Zehnder interferometer (MZI), comprised of PBS2, PBS3, and a set of plane mirrors, M1–6. The delay stage matches the path lengths of the two arms of the MZI. The spiral-phase plate (SPP) transforms the Gaussian beam into a vortex beam of order l_p. Upon recombination on PBS3, the horizontally (H) polarized vortex beam and the vertically (V) polarized Gaussian beam produce [2] an FP beam, represented as $E_p = \alpha_p |E_p^H, l_p\rangle + \beta_p |E_p^V, 0\rangle$, where α_p and β_p are the
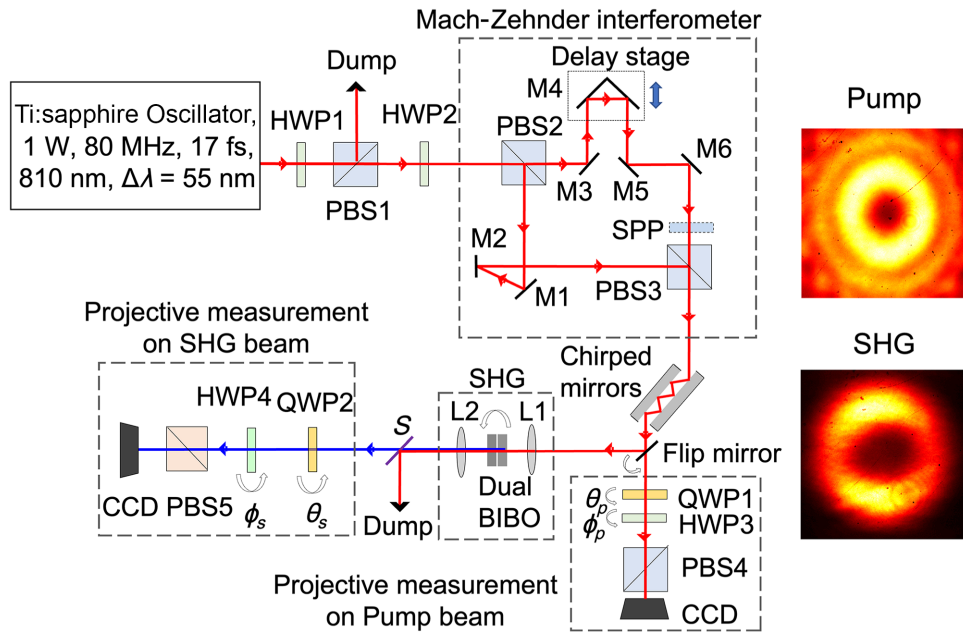
FIG. 2. The experimental setup for SHG of an FP beam: HWP1–4, $\lambda/2$ plates; PBS1–5, polarizing-beam-splitter cubes; SPP, spiral-phase plate; QWP1 and 2, $\lambda/4$ plates; M1–6, mirrors; L1 and 2, lenses; S, wavelength separator; CCD, camera; dual BIBO, nonlinear crystal. The intensity profiles of the pump and the SH FP beams.

amplitude coefficients of the vortex beam and Gaussian beam, respectively, and $\alpha_p^2 + \beta_p^2 = 1$. Using the SPPs of the phase winding corresponding to vortex orders $l_p = 1$–3, we generate FP beams of order up to 3. A pair of chirped mirrors compensate the stretching of the ultrafast FP beam resulting from the dispersion of the optical components. The flip mirror directs the pump beam either to the second-harmonic (SH) setup or to the projective-measurement setup comprised of a $\lambda/4$ plate (QWP1), a $\lambda/2$ plate (HWP3), PBS4, and a CCD camera for polarization and Stokes parameters. The lens L1, of focal length $f_1 = 150$ mm, is used to focus the pump at the center of the dual-BiB$_3$O$_6$ (BIBO) crystal, consisting of two contiguous BIBO crystals, each having a thickness of 0.6 mm and an aperture of 1×1 cm^2, with an orthogonal optic axis [37]. Both crystals are cut at an angle, $\theta = 151.7^0$ ($\phi = 90^0$), in the optical y-z plane for type-I ($e + e \rightarrow o$) phase-matching for the frequency doubling of 810 nm into 405 nm [20]. The unique geometry of the dual-BIBO crystal permits single-pass frequency doubling of the orthogonally polarized components of the FP beam. Lens L2, of focal length $f2 = 100$ mm, collimates the fundamental and SHG beams. Subsequently, the polarization and Stokes parameters of the SH beam extracted from the pump by the harmonic separator, S, are measured with the aid of the projective-measurement [41] setup comprised of a $\lambda/4$ plate (QWP2), a $\lambda/2$ plate (HWP4), PBS5, and a CCD camera. The inset of Fig. 2 shows a typical intensity profile of the pump and SH FP beams.

IV. RESULTS

A. Polarization structure

To verify the pump FP beam, we record the intensity distribution of the beam using different combinations of the angles of QWP1 and HWP3 and calculate the Stokes parameters, S_1, S_2, and S_3. Using the Stokes parameters, we calculate the orientation (ψ) and ellipticity (χ) [41] of the polarization ellipse with the results shown in Fig. 3. As is evident from Fig. 3(a), the transverse distribution of the polarization ellipse of the pump beam of vortex order $l_p = 1$ contains a pair of C-point polarization singularity consisting of a lemon (see the black circle) and a star (see the black square) and a single L line (green line), confirming the vortex order of the FP beam to be $l_p = 1$. To verify the experimental results, we theoretically calculate the polarization-ellipse distribution of the pump FP beam. However, in the current experiment, the Ti:sapphire laser produces the output beam in an elliptical Gaussian-beam spatial profile. While spatial filtering can easily transform the elliptical beam into a high-quality Gaussian beam at the cost of overall laser power, the demand for higher laser power for the SHG process restricts us from using any mode filtering. To address such limitations and to find a close match with the experimental results, we modify the electric field equation of the FP beam to accommodate the ellipticity of the laser beam as follows:

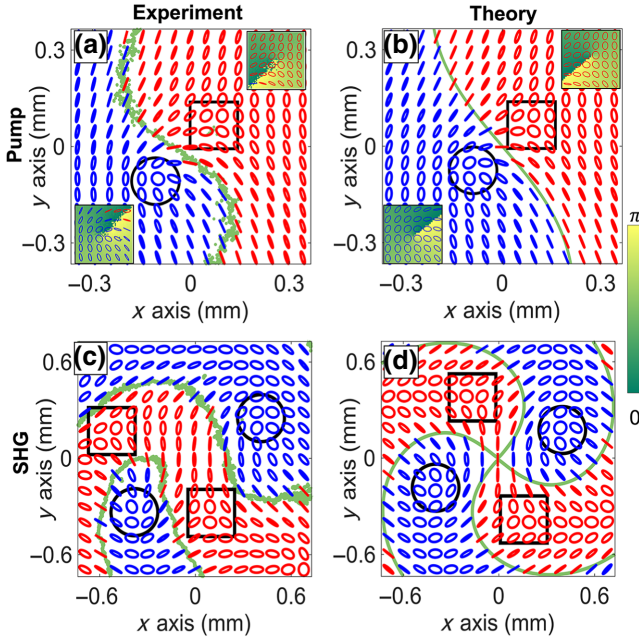$$E = \alpha \, |E^H, l\rangle + \beta \, |E^V, 0\rangle$$

FIG. 3. The (a) experimental and (b) theoretical transverse polarization distribution of the FP pump beam of vortex order $|l_p| = 1$. The experimental parameters used for the theoretical calculation are as follows: beam widths, $w_{xl} = 1.2$ mm, $w_{yl} = 1.3$ mm, $w_{x0} = 2.9$ mm, and $w_{y0} = 5.3$ mm; relative intensities, $(\alpha_p^2, \beta_p^2) = (0.75, 0.25)$. (c),(d) The (c) experimental and (d) theoretical polarization distribution of the corresponding SHG of vortex order $|l_{sh}| = 2$, using the following experimental parameters: beam widths $w_{xl} = 1.6$ mm, $w_{yl} = 1.9$ mm, $w_{x0} = 1.7$ mm, and $w_{y0} = 4$ mm; relative intensities, $(\alpha_{shg}^2, \beta_{shg}^2) = (0.26, 0.74)$. The inset images are enlargements of the lemon and star (C-point) singularities highlighted by the black circle and square, respectively. The background of the inset is the ellipse orientation and the green lines depict the L lines.

$$= E_{LG} \left(\frac{\sqrt{2}r}{w_0} \right)^{|l|} LG_l (2r_l^2) \exp\left(\frac{-ikr^2}{2R_1} - r_l^2 + il\phi \right) \hat{\mathbf{H}}$$

$$+ E_G \exp\left(\frac{-ikr^2}{2R_2} - r_0^2 \right) \hat{\mathbf{V}}.$$

Here, α_p and β_p, the amplitude coefficients of the vortex beam and the Gaussian beam, respectively, and $\alpha_p^2 + \beta_p^2 = 1$ are calculated using the intensity profile of the constituent beams and the subsequently estimated electric-field-amplitude terms E_{LG} and E_G. The terms $r_l = \sqrt{(x/w_{xl})^2 + (y/w_{yl})^2}$ and $r_0 = \sqrt{(x/w_{x0})^2 + (y/w_{y0})^2}$ represent the asymmetry of the LG and Gaussian beams, having beam widths along the x and y axes of w_{xl}, w_{yl}, and w_{x0}, w_{y0}, respectively. All these parameters are calculated using the experimentally measured spatial profiles of the Gaussian and LG beams. These electric field expressions are later utilized for

calculating the Stokes parameters S_1, S_2, and S_3. The theoretically calculated polarization distribution of the pump [see Fig. 3(b)] contains a pair of C-point and single L-line singularities and is in close agreement with the experimental results. The insets of Figs. 3(a) and 3(b) show enlarged images of the lemon and star singularities, with the ellipse orientation as the background color map. The parameters used for the theoretical calculations are given in the caption.

Similarly, we calculate the experimental and theoretical polarization distribution of the single-pass SHG of the pump beam of $l_p = 1$. For the theoretical simulation, the single-pass efficiency of the dual crystal is calculated directly from the intensity output of the individual Gaussian and LG beams. This indirect approach allows us to effectively account for various parameters that affect the efficiency of the SHG, apart from the nonlinear efficiency. One of the major parameters is the slight variation in the focal length of the Gaussian and LG beams arising from the different divergence during propagation. This slight focal change variation is essential, since the thin crystal is used in the experiment. Furthermore, to reduce the effect of this factor, we optimize the focal length of the focusing lens L1 to 150 mm at the cost of SHG efficiency. The second factor that affects the SHG efficiency is the optimization that emerges from simultaneously satisfying the critical phase matching of the dual crystal. Since each of the crystals in the dual-crystal scheme requires a pitch and yaw angle, it is cumbersome to accommodate such parameters in the theoretical model but relatively easy to optimize the experimental setup. From the relative intensity and beam size obtained from the individual Gaussian and LG beam calculations, we theoretically calculate the polarization distribution. As evident from Figs. 3(c) and 3(d), the polarization distribution (experimental and theoretical) of the SHG beam contains two pairs of C points and two L lines, confirming the vortex order of the SHG beam to be $l_{sh} = 2$, twice that of the pump beam. Such an observation confirms the doubling of the OAM mode or the C-point and L-line singularities of the pump beam in the SHG process [42]. The doubling of C-point (marked by the black circle and square) and L-line (green line) singularities in the SHG process can be understood as follows. As reported previously [20], the dual-BIBO crystal converts the pump beam of the electric field, $E_p = \alpha_p |E_p^H, l_p\rangle + \beta_p |E_p^V, 0\rangle$, into the SH beam of the electric field, $E_{sh} = \alpha_{sh} |E_{sh}^V, 2l_p\rangle + \beta_{sh} |E_{sh}^H, 0\rangle$. Here, α_{sh} and β_{sh} are the amplitude coefficients of the vortex and Gaussian SH beams, respectively, governed by the conversion efficiency of the individual beams. The relative phase due to the birefringence properties of the crystal is controlled by the time delay between the orthogonal components of the pump FP beam.

Furthermore, using the FP beam of vortex order $l_p = 3$, we measure the Stokes parameters, S_1, S_2, and S_3, for
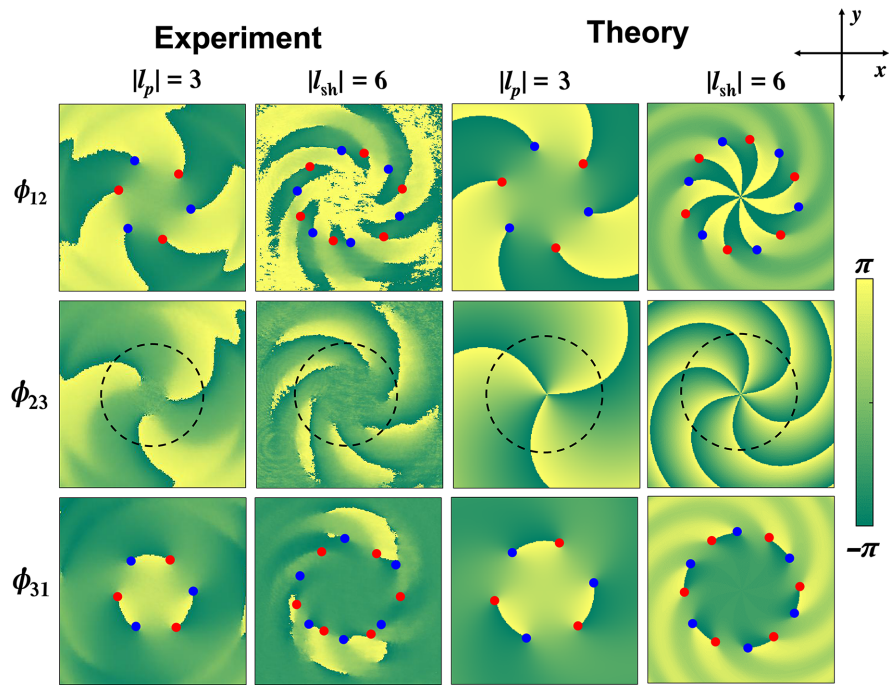
FIG. 4. The experimental Stokes phases, ϕ_{12}, ϕ_{23}, and ϕ_{31}, of the pump (first column) and SHG (second column) FP beams, together with the theoretical Stokes phases, ϕ_{12}, ϕ_{23}, and ϕ_{31} of the pump (third column) and SHG (fourth column) FP beams. The dotted circle is a guide to the observation of phase winding.

the pump and the corresponding SH beam and we subsequently calculate the Stokes phases, ϕ_{12}, ϕ_{23}, and ϕ_{31}. The results are shown in Fig. 4. As is evident from the first column of Fig. 4, the Stokes phase ϕ_{12}, representing the *C*-point singularity, contains three pairs of points marked by blue and red dots, having phase winding corresponding to the charge $\sigma_{12} = +1$ (star singularity) and $\sigma_{12} = -1$ (lemon singularity), respectively. Using the formula $\sigma_{12} = 2I_c$, the singularity indices I_c of the *C* points are found to be $I_c = +1/2$ and $I_c = -1/2$, respectively. The Stokes phase ϕ_{23} of the FP beam shows azimuthal phase winding corresponding to the vortex order $l_p = 3$ of the pump beam. Therefore, the vortex order of the FP beam can be determined from the Stokes phase ϕ_{23}. On the other hand, the Stokes phase ϕ_{31} represents three pairs of singularities over a ring. The second column of Fig. 4 shows the Stokes phases ϕ_{12}, ϕ_{23}, and ϕ_{31} of the SHG beam of the FP beam of vortex order $l_p = 3$. As is evident from the second column of Fig. 4, the Stokes phase ϕ_{12} has six pairs (lemon, blue; star, red) of *C*-point singularities with singularity indices $I_c = +1/2$ and $I_c = -1/2$, respectively, confirming the doubling of the *C*-point singularities in the SHG process. On the other hand, the Stokes phase ϕ_{23} shows azimuthal phase winding corresponding to the vortex charge, $\sigma_{23} = l_{sh} = 6$, twice the order of the pump-vortex charge, $l_p = 3$, of the FP beam owing to the OAM conservation in the nonlinear frequency-doubling processes. Similarly, we observe six pairs of singularities

over a ring in the Stokes phase ϕ_{31} of the SH FP beam. To support the experimental results, we perform a theoretical calculation for each of the Stokes phases for the pump by accommodating the experimental parameters $w_{xl} = 1.2$ mm, $w_{yl} = 1.7$ mm, $w_{x0} = 2.9$ mm, $w_{y0} = 2.5$ mm, and $(\alpha_p^2, \beta_p^2) = (0.75, 0.25)$. Furthermore, for SHG, we use the parameters $w_{xl} = 1.9$ mm, $w_{yl} = 1.8$ mm, $w_{x0} = 0.9$ mm, $w_{y0} = 1.1$ mm, and $(\alpha_{shg}^2, \beta_{shg}^2) = (0.35, 0.65)$ for calculating the Stokes phases of SHG. The theoretically calculated Stokes phases of the pump and the corresponding SHG FP beam, as shown in the third and fourth columns of Fig. 4, respectively, are in close agreement with the experimental results. From the results shown in Fig. 4, it is evident that the polarization properties of the FP beams are conserved in nonlinear processes and the Stokes phases can be explored as important tools to characterize the nonlinear optical processes.

To understand the dynamics of the *C*-point singularities for the different relative intensities of the constituent modes, we measure the Stokes parameters for both the pump and the SHG beams while changing the relative intensities, α_p^2 and $\beta_p^2 = 1 - \alpha_p^2$, of the vortex and Gaussian beams, respectively, of the FP pump beam and calculate the Stokes phase ϕ_{12}, with the results shown in Fig. 5. As is evident from the first row of Fig. 5, the Stokes phase ϕ_{12} of the pump beam maintains a uniform phase distribution for $(\alpha_p^2, \beta_p^2) = (0, 1)$ and $(1, 0)$ due to the absence of orthogonal polarization states. However, the distribution
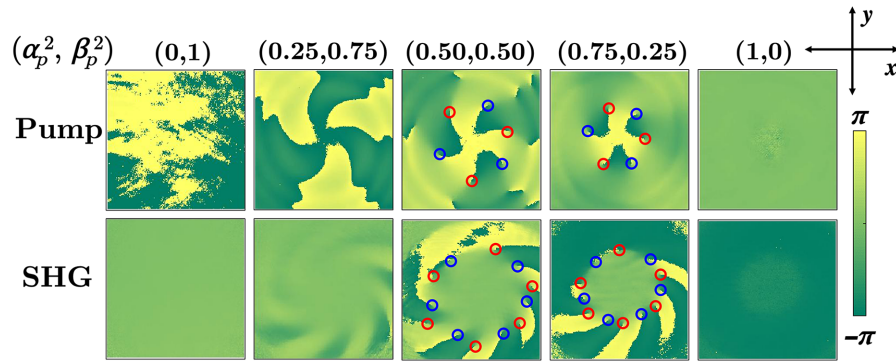
FIG. 5. The variation of the Stokes phase ϕ_{12} of the pump (first row) and the SH FP beam (second row) for different combinations of (α_p^2, β_p^2).

of the Stokes phase ϕ_{12} changes with the combination of $(\alpha_p^2$ and $\beta_p^2)$ values, showing the presence of three pairs of lemon and star singularities for $(\alpha_p^2, \beta_p^2) = (0.5, 0.5)$ and $(0.75, 0.25)$. The distribution of the Stokes phase ϕ_{12} of the SHG beam, as shown in the second row of Fig. 5, follows the Stokes-phase distribution of the pump beam, with six pairs of lemon and star singularities for $(\alpha_p^2, \beta_p^2) = (0.5, 0.5)$ and $(0.75, 0.25)$. It is evident from the first and second rows of Fig. 5 that the increase of α_p^2 (the vortex-beam intensity) brings the singularity points (lemon and star) toward the center and they finally annihilate each other to form the uniform Stokes-phase, ϕ_{12}, distribution.

B. Coverage

We further study the polarization coverage of the pump and the corresponding SH FP beams. Using the pump FP
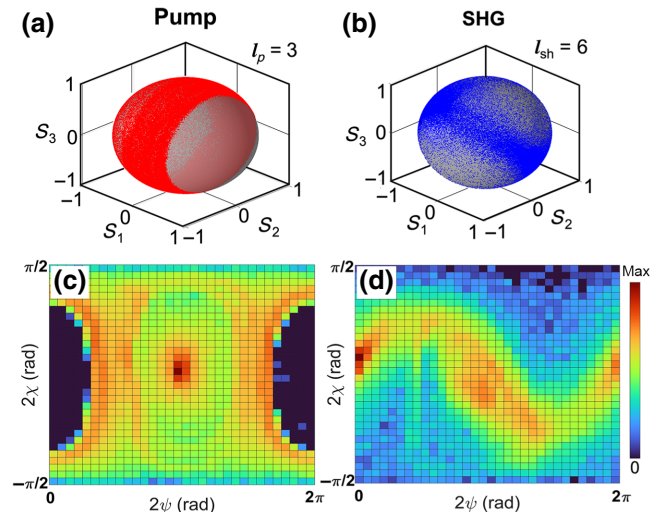

FIG. 6. (a),(b) The Stokes parameters of (a) the pump and (b) the SH FP beams of pump vortex order $l_p = 3$, projected onto the surface of the Poincaré sphere for $(\alpha_p^2, \beta_p^2) = (0.5, 0.5)$. (c),(d) The distribution of the polarization states in the 2ψ-2χ plane for (c) pump and (d) SH FP beams.

beam of order $l_p = 3$ and $(\alpha_p^2, \beta_p^2) = (0.5, 0.5)$, we calculate the Stokes parameters of the pump and the SHG beam and project them on the surface of the Poincaré sphere, with the results shown in Figs. 6(a) and 6(b), respectively. As is evident from Figs. 6(a) and 6(b), the polarization states on the Poincaré sphere have a complicated distribution, with void regions. Therefore, it is not easy to estimate the polarization coverage of the FP beam using the conventional area-integration method [40]. As such, one can transform the three-dimensional (3D) surface onto the 2D plane and estimate the polarization coverage. However, in doing so, one has to make the necessary correction to encounter the distortion effect commonly observed while transforming the surface of a sphere into a flat plane, especially for the sections in the pole region of the surface; a rectangle near the poles corresponds to a smaller area on the sphere than a rectangle near the equator. On the other hand, each discrete point on the surface of the Poincaré sphere represented by the Stokes parameters S_1, S_2, and S_3 in Cartesian coordinates can also be represented by the ellipse orientation, ψ, the ellipticity, χ, and the Stokes parameter, S_0, in spherical coordinates. Therefore, the polarization states represented on the surface of the Poincaré sphere can also be represented in rectangular Cartesian coordinates by considering the x and y axes as 2ψ and 2χ, with the limits $\psi \in [0, \pi]$ and $\chi \in [-\pi/4, +\pi/4]$, respectively. In doing so, one can transform the polarization states commonly depicted on the curved surface into a 2D plain surface.

Figures 6(c) and 6(d) represent the distribution of polarization states in the 2ψ-2χ plane for beams having the polarization states shown in Figs. 6(a) and 6(b), respectively. Now, to calculate the polarization coverage of the beams, we divide the 2D polarization map of length $2\psi \in [0, 2\pi]$ and breadth $2\chi \in [-\pi/2, +\pi/2]$ containing all polarization states of the beam into N_0 sections or buckets of equal area. In this case, each of the buckets contains different polarization states of the beam. Since the polarization state of the beam is measured pixel-wise using the
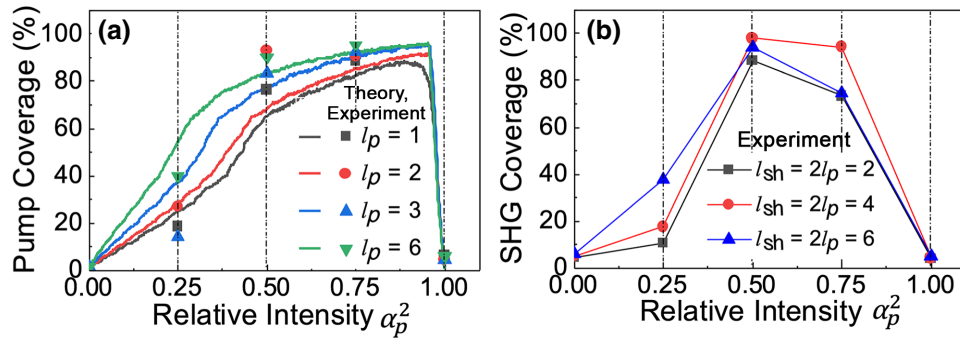
FIG. 7. The variation of the polarization coverage (a) of the pump and (b) of the corresponding SH Poincaré beams of different pump-vortex orders for a different combination of (α_p^2, β_p^2) values. The solid lines are theoretical results.

recorded intensity profile of the beam, it might happen that many pixels can show identical polarization states. This is made evident in Figs. 6(a) and 6(b). As a result, a single bucket can carry multiple data points, which are also shown by the color maps (black means no points, while red denotes the maximum data points) in Figs. 6(c) and 6(d). However, the number of data points in a bucket does not contribute to the polarization coverage. Therefore, we consider the bucket as being full if the corresponding polarization state is detected in one or more data points. Now, if the number of buckets containing at least one point is N, then the polarization coverage of the beam can be calculated as $100 \times N/N_0$. For a beam with 100% polarization coverage, N should be equal to N_0. However, proper selection of the number of buckets is very important. For example, suppose that we consider N to be small. In that case, the bucket size will be large enough to cover the area that does not have any polarization state of the beam and the polarization coverage of the beam will be overestimated. On the other hand, if N is very large, then the bucket size will be small and fewer buckets will carry a polarization state with respect to the total number of buckets, thus underestimating the result. Therefore, to optimize the number of buckets, N, we lock the least count of the area measurement to be 0.1%. Such a small value of the least count can be obtained by dividing the areas of the square-shaped 2ψ-2χ plane by $N = n \times n \sim 1000$ buckets. Therefore, we consider $n \sim 32$ and measure the polarization coverage of the pump FP beam of order $l_p = 1$, 2, 3, and 6 while varying the value of (α_p^2, β_p^2). The results are shown in Fig. 7(a). As is evident from Fig. 7(a), the polarization coverage of the FP beam of all orders lies in the range of 75–95% for $(\alpha_p^2, \beta_p^2) = (0.5, 0.5)$ and $(0.75, 0.25)$ and around 1% for $(\alpha_p^2, \beta_p^2) = (0, 1)$ and $(1, 0)$. The low coverage (approximately 1%) can be attributed to the absence of both polarization states in the beam. On the other hand, for $(\alpha_p^2, \beta_p^2) = (0.25, 0.75)$, the polarization coverage varies in the range of 20–40% for all vortex orders, indicating that in the presence of the azimuthal phase, the relative intensity of the vortex beam plays a crucial role in the polarization

coverage of the FP beams. Using the experimental parameters, we also calculate the polarization coverage of FP beams of different orders.

As is evident from Fig. 7(a), the experimental polarization coverage represented as dots on the plot lies very close to the theory, which is shown by the lines in the plots for FP beams of all orders. However, the small deviation in the experimental and theoretical results can be attributed to the asymmetry in the spatial profiles of the experimental beams. The maximum error for the polarization coverage measurement is the same as the least-count area, 0.1%, used in this study. We also measure the polarization coverage of the SH FP beam for pump orders $l_p = 1$, 2, and 3, for different values of (α_p^2, β_p^2), with the results shown in Fig. 7(b). Interestingly, from Fig. 7(b), we see that the best weightings for the fundamental field do not give optimal coverage for all topological charges. For example, the relative weight of 0.25 has the best coverage for $l_{sh} = 6$ but this changes for relative weights of 0.75, where the best coverage is given for $l_{sh} = 4$. When the relative weight is increased above 0.5, we then see a decrease in SHG coverage. This indicates that the size mismatch between the SHG vortex component and the Gaussian component has a bigger influence. This size mismatch comes from the fact that the SHG of the Gaussian component has a waist-resizing effect of a factor of the square root of 2 and this can be seen as a circle getting shrunk, while the phase vortex component can be seen as a ring becoming thinner. Ultimately, this decreases the overlap between the modes and, thus, the accessible states of polarization and coverage. A striking consequence is that, for topological charge 6 and relative weighting 0.75, the fundamental beam is a FP beam, as it is above the threshold of 75% coverage, but if the same beam is generated through the SHG of a FP beam of $l_p=3$ with the same weights, it falls below the threshold of 75% and is no longer considered a FP beam. When comparing the coverage of the pump and SHG for the same α values, we note that while the pump coverage increases for values higher than 0.5, the SHG coverage decreases. This means that,
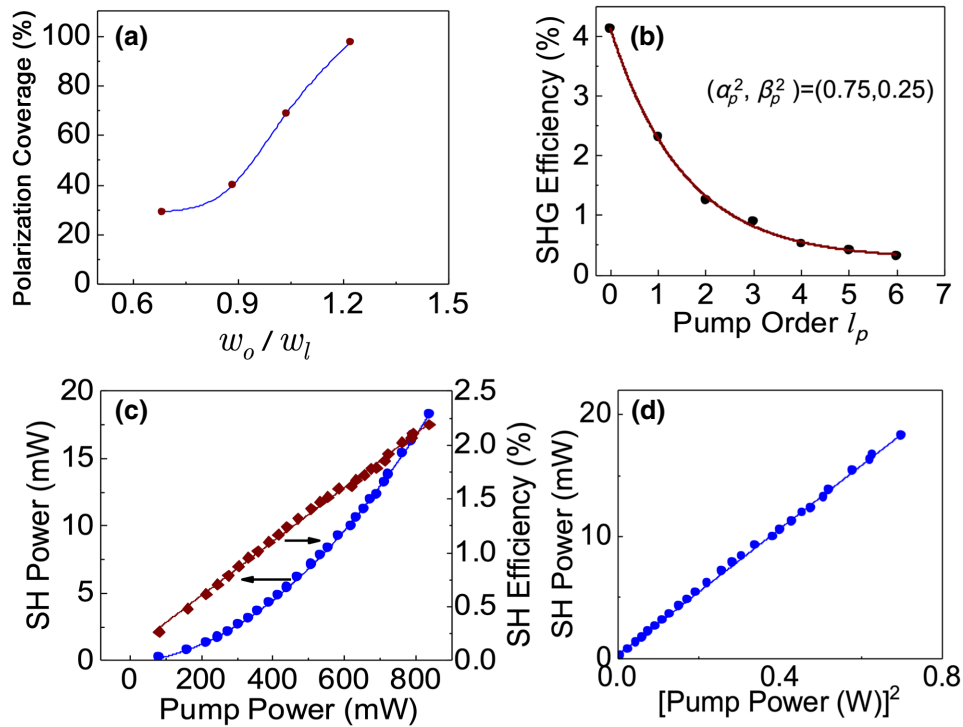
FIG. 8.   (a) The variation of the pump-polarization coverage with the relative full width at half maximum (FWHM) of the Gaussian and vortex beams. (b) The variation of the SHG efficiency with the vortex order of the FP beams. (c) The variation of SH power (blue) and the SH efficiency (brown) with the input power of the FP beams of vortex order $l_p = 1$. (d) The dependence of the SH power on the square of the pump power. The lines are guides to the eyes.

counterintuitively, by decreasing the coverage of the pump beam, it is possible to increase the coverage for the SHG. Since the beam size of the Gaussian beam reduces and the LG beam size increases during the SHG process, it is difficult to maintain the spatial overlap between the two beams and generate the FP beam for the higher order. So, we note that for any lower-order modal combination of FP beams, we are able to experimentally control the coverage on the Poincaré sphere from 0 to 100% continuously by adjusting the relative intensity between the two modes.

To observe the effect of the size of the constituent beams of the FP beam on the polarization coverage, we vary the pump-beam waist of the Gaussian beam (w_0) from 2.1 mm to 3.6 mm and measure the pump polarization coverage while keeping the annular width (full width at half maximum, FWHM) (w_1) of the vortex beam of order $l = 1$ constant (3 mm) and $\alpha^2 = 0.9$. The results are shown in Fig. 8(a). As expected, the polarization coverage increases from 29.3% for $w_0/w_l = 0.7$ to a maximum of 97.75% at $w_0/w_l = 1.2$. However, our numerical simulations [see Fig. 7(a)] show that the range of polarization coverage as a function of the beam-width ratio decreases with the decrease in the intensity ratio α^2/β^2. Therefore, in our study, we use ($\alpha^2 = 0.9$, $\beta^2 = 0.1$) to observe the higher control of the polarization coverage using the beam-width

ratio. Unfortunately, under an intensity ratio such as α^2/β^2, the conversion efficiency of the Gaussian beam is so low that the FP beam becomes a scalar vortex beam. On the other hand, optimization of the intensity ratio results in almost constant polarization coverage in SHG with varying beam-waist ratios. Therefore, a systematic study while considering the conversion efficiency of the constituent beams is essential to observe the large variation of the polarization coverage in the SHG process. We also measure the SHG efficiency of the FP pump beam of different orders, with the results shown in Fig. 8(b). As observed in Fig. 8(b), the single-pass SHG efficiency of the FP beam decreases with the vortex order from 4.19% for $l_p = 0$ (Gaussian beam with diagonal polarization) to 0.32% for $l_p = 6$, similar to the single-pass SHG of the vortex beam [42], due to the increase of the dark-core size with the vortex order. Keeping $(\alpha_p^2, \beta_p^2) = (0.5, 0.5)$, we measure the power scaling of the FP beam of order $l_p = 1$, with the results shown in Fig. 8(c). As is evident from Fig. 8(c), the output power and the SH efficiency increase quadratically and linearly, respectively, with the pump power, producing a maximum average output power of 18.3 mW at a single-pass conversion efficiency as high as 2.19% without any sign of saturation. The linear variation of the SH power with the square of the pump power, as shown in

Fig. 8(d), further confirms the possibility of generating an SH FP beam of higher average power with an increase of the pump power.

V. CONCLUSIONS

In conclusion, we study the nonlinear generation of ultrafast FP beams while preserving the polarization characteristics of the pump FP beam and validate our experimental findings with theory. Analysis of the Stokes parameters and the Stokes phases reveals the conservation of *C*-point and *L*-line singularities in nonlinear processes. Even though beams having spatially varying polarization are being utilized in a wide variety of applications, the effective measurement and control of the accessible polarization state has not been explored. In this work, we devise a method to estimate the polarization coverage of the FP beam, which can be extended to any optical beam with spatially varying polarization. Furthermore, we show that the variation of the polarization coverage for different intensity weightings of the constituent beams controls the available polarization state in an optical beam. We also show that through SHG of the FP beam, we can further control the accessible polarization while converting the beam into a new wavelength. The control of accessible polarization states via nonlinear interaction can be effectively utilized in applications that require short wavelengths without the requirement of any new optical elements in the new wavelength. It is also interesting to note that the SHG FP beam has the highest polarization coverage for equal weightings between the beams in the fundamental frequency. We also devise a method to control the effective polarization of the FP beam through SHG, which will hopefully be a very useful tool for applications demanding short wavelengths, which are widely accessed through SHG. Additionally, it is observed in the literature that the FP beams have smaller scintillation than comparable beams of uniform polarization in the presence of atmospheric turbulence [43,44]. The robustness of the FP beams against atmospheric turbulence can be further understood by studying the change in the overall polarization coverage of such beams during free-space propagation and helping to design the optimum special polarization structured beams for such applications. The current polarization-coverage measurement technique can also be useful to study the manipulation of Poincaré beams on the different parts of the Poincaré sphere [45].

[1] A. Forbes, M. de Oliveira, and M. R. Dennis, Structured light, Nat. Photonics **15**, 253 (2021).

[2] A. M. Beckley, T. G. Brown, and M. A. Alonso, Full Poincaré beams, Opt. Express **18**, 10777 (2010).

[3] C. Rosales-Guzmán, B. Ndagano, and A. Forbes, A review of complex vector light fields and their applications, J. Opt. **20**, 123001 (2018).

[4] E. Otte, C. Alpmann, and C. Denz, Polarization singularity explosions in tailored light fields, Laser Photon. Rev. **12**, 1700200 (2018).

[5] T. Bauer, P. Banzer, E. Karimi, S. Orlov, A. Rubano, L. Marrucci, E. Santamato, R. W. Boyd, and G. Leuchs, Observation of optical polarization Möbius strips, Science **347**, 964 (2015).

[6] B. Ndagano, B. Perez-Garcia, F. S. Roux, M. McLaren, C. Rosales-Guzman, Y. Zhang, O. Mouane, R. I. Hernandez-Aranda, T. Konrad, and A. Forbes, Characterizing quantum channels with non-separable states of classical light, Nat. Phys. **13**, 397 (2017).

[7] W. Han, W. Cheng, and Q. Zhan, Flattop focusing with full Poincaré beams under low numerical aperture illumination, Opt. Lett. **36**, 1605 (2011).

[8] A new twist for materials science: The formation of chiral structures using the angular momentum of light, Adv. Opt. Mater. **7**, 1801672 (2019).

[9] C. He, H. He, J. Chang, B. Chen, H. Ma, and M. J. Booth, Polarisation optics for biomedical and clinical applications: A review, Light: Sci. Appl. **10**, 194 (2021).

[10] E. Otte and C. Denz, Optical trapping gets structure: Structured light for advanced optical manipulation, Appl. Phys. Rev. **7**, 041308 (2020).

[11] A. Forbes, Structured light from lasers, Laser Photon. Rev. **13**, 1900140 (2019).

[12] D. Naidoo, F. Roux, A. Dudley, I. Litvin, B. Piccirillo, L. Marrucci, and A. Forbes, Controlled generation of higher-order Poincaré sphere beams from a laser, Nat. Photonics **10**, 327 (2016).

[13] N. Abraham and W. Firth, Overview of transverse effects in nonlinear-optical systems, JOSA B **7**, 951 (1990).

[14] Y. Shen, X. Yang, D. Naidoo, X. Fu, and A. Forbes, Structured ray-wave vector vortex beams in multiple degrees of freedom from a laser, Optica **7**, 820 (2020).

[15] J. Pinnell, I. Nape, B. Sephton, M. A. Cox, V. Rodríguez-Fajardo, and A. Forbes, Modal analysis of structured light with spatial light modulators: A practical tutorial, JOSA A **37**, C146 (2020).

[16] W. T. Buono and A. Forbes, Nonlinear optics with structured light, Opto-Electron. Adv. **5**, 210174 (2022).

[17] J. Courtial, K. Dholakia, L. Allen, and M. Padgett, Second-harmonic generation and the conservation of orbital angular momentum with high-order Laguerre-Gaussian modes, Phys. Rev. A **56**, 4193 (1997).

[18] W. Buono, L. Moraes, J. Huguenin, C. Souza, and A. Khoury, Arbitrary orbital angular momentum addition in second harmonic generation, New J. Phys. **16**, 093041 (2014).

[19] L. Zhang, X. Qiu, F. Li, H. Liu, X. Chen, and L. Chen, Second harmonic generation with full Poincaré beams, Opt. Express **26**, 11678 (2018).

[20] R. K. Saripalli, A. Ghosh, N. Apurv Chaitanya, and G. Samanta, Frequency-conversion of vector vortex beams with space-variant polarization in single-pass geometry, Appl. Phys. Lett. **115**, 051101 (2019).

[21] H. Liu, H. Li, Y. Zheng, and X. Chen, Nonlinear frequency conversion and manipulation of vector beams, Opt. Lett. **43**, 5981 (2018).

[22] H.-J. Wu, B. Zhao, C. Rosales-Guzmán, W. Gao, B.-S. Shi, and Z.-H. Zhu, Spatial-Polarization-Independent

Parametric Up-Conversion of Vectorially Structured Light, Phys. Rev. Appl. **13**, 064041 (2020).

[23] C. Yang, Z.-Y. Zhou, Y. Li, Y.-H. Li, S.-L. Liu, S.-K. Liu, Z.-H. Xu, G.-C. Guo, and B.-S. Shi, Nonlinear frequency conversion and manipulation of vector beams in a Sagnac loop, Opt. Lett. **44**, 219 (2019).

[24] Z.-C. Ren, Y.-C. Lou, Z.-M. Cheng, L. Fan, J. Ding, X.-L. Wang, and H.-T. Wang, Optical frequency conversion of light with maintaining polarization and orbital angular momentum, Opt. Lett. **46**, 2300 (2021).

[25] H.-J. Wu, B.-S. Yu, Z.-H. Zhu, W. Gao, D.-S. Ding, Z.-Y. Zhou, X.-P. Hu, C. Rosales-Guzmán, Y. Shen, and B.-S. Shi, Conformal frequency conversion for arbitrary vectorial structured light, Optica **9**, 187 (2022).

[26] N. R. da Silva, A. de Oliveira, M. Arruda, R. M. de Araújo, W. Soares, S. Walborn, R. Gomes, and P. S. Ribeiro, Stimulated Parametric Down-Conversion with Vector Vortex Beams, Phys. Rev. Appl. **15**, 024039 (2021).

[27] B. Sephton, A. Vallés, I. Nape, M. A. Cox, F. Steinlechner, T. Konrad, J. P. Torres, F. S. Roux, and A. Forbes, High-dimensional spatial teleportation enabled by nonlinear optics, arXiv preprint arXiv:2111.13624 (2021).

[28] V. Jarutis, A. Matijošius, V. Smilgevičius, and A. Stabinis, Second harmonic generation of higher-order Bessel beams, Opt. Commun. **185**, 159 (2000).

[29] D. Ding and J.-y. Lu, Second-harmonic generation of the *n*th-order Bessel beam, Phys. Rev. E **61**, 2038 (2000).

[30] K. Shinozaki, C.-q. Xu, H. Sasaki, and T. Kamijoh, A comparison of optical second-harmonic generation efficiency using Bessel and Gaussian beams in bulk crystals, Opt. Commun. **133**, 300 (1997).

[31] J. Arlt, K. Dholakia, L. Allen, and M. Padgett, Efficiency of second-harmonic generation with Bessel beams, Phys. Rev. A **60**, 2438 (1999).

[32] V. Magni, Optimum beam for second harmonic generation, Opt. Commun. **176**, 245 (2000).

[33] R. L. Phillips and L. C. Andrews, Spot size and divergence for Laguerre Gaussian beams of any order, Appl. Opt. **22**, 643 (1983).

[34] S. Shwartz, M. Fuchs, J. B. Hastings, Y. Inubushi, T. Ishikawa, T. Katayama, D. A. Reis, T. Sato, K. Tono, M. Yabashi, S. Yudovich, and S. E. Harris, X-Ray Second Harmonic Generation, Phys. Rev. Lett. **112**, 163901 (2014).

[35] H. Kerdoncuff, J. B. Christensen, and M. Lassen, Quantum frequency conversion of vacuum squeezed light to bright tunable blue squeezed light and higher-order spatial modes, Opt. Express **29**, 29828 (2021).

[36] N. Gisin, G. Ribordy, W. Tittel, and H. Zbinden, Quantum cryptography, Rev. Mod. Phys. **74**, 145 (2002).

[37] M. Jabir, N. Apurv Chaitanya, M. Mathew, and G. Samanta, Direct transfer of classical non-separable states into hybrid entangled two photon states, Sci. Rep. **7**, 1 (2017).

[38] I. Freund, Poincaré vortices, Opt. Lett. **26**, 1996 (2001).

[39] I. Freund, A. Mokhun, M. Soskin, O. Angelsky, and I. Mokhun, Stokes singularity relations, Opt. Lett. **27**, 545 (2002).

[40] G. Arora, Ruchi, and P. Senthilkumaran, Full Poincaré beam with all the Stokes vortices, Opt. Lett. **44**, 5638 (2019).

[41] D. H. Goldstein, *Polarized Light* (CRC Press, Boca Raton, USA, 2017).

[42] N. A. Chaitanya, A. Aadhi, M. Jabir, and G. K. Samanta, Frequency-doubling characteristics of high-power, ultrafast vortex beams, Opt. Lett. **40**, 2614 (2015).

[43] Y. Gu, O. Korotkova, and G. Gbur, Scintillation of nonuniformly polarized beams in atmospheric turbulence, Opt. Lett. **34**, 2261 (2009).

[44] C. Wei, D. Wu, C. Liang, F. Wang, and Y. Cai, Experimental verification of significant reduction of turbulence-induced scintillation in a full Poincaré beam, Opt. Express **23**, 24331 (2015).

[45] X. Sun, Y. Geng, Q. Zhu, W. Huang, Y. Zhang, W. Wang, and L. Liu, Unitary transformation for Poincaré beams on different parts of Poincaré sphere, Sci. Rep. **10**, 14251 (2020).